





Shape memory alloy-based 3D morphologically reconfigurable chiral metamaterial for tailoring circular dichroism by voltage control

LIXIN JIANG,^{1,†}  QI YUAN,^{1,†}  HAO YANG,^{1,†} YONGFENG LI,^{1,3} LIN ZHENG,¹ ZHIBIAO ZHU,¹ 
SHUANG LIANG,¹ YONGQIANG PANG,² HE WANG,^{1,4}  JIAFU WANG,¹ AND SHAOBO QU¹

¹Shaanxi Key Laboratory of Artificially-Structured Functional Materials and Devices, Airforce Engineering University, Xi'an 710051, China

²Electronic Materials Research Laboratory, Key Laboratory of the Ministry of Education, Xi'an Jiaotong University, Xi'an 710049, China

³e-mail: liyf217130@126.com

⁴e-mail: 18066540235@163.com

Received 17 November 2022; revised 21 December 2022; accepted 28 December 2022; posted 5 January 2023 (Doc. ID 480979); published 13 February 2023

Three-dimensional chiral materials with intrinsic chirality play a crucial role in achieving a strong chiral response and flexible light manipulation. Reconfigurable chirality through the 3D morphological transformation of chiral materials is significant for greater freedom in tailoring light but remains a challenge. Inspired by the unique 3D morphological memory capability of shape memory alloys (SMAs), we demonstrate and discuss a chiral resonator in the microwave regime that can realize reconfigurable chirality through 3D morphological transformation. The introduction of heating film realizes voltage control of SMA's morphology for utilizing the temperature sensitivity of SMA better, enabling arbitrary control of circular dichroism (CD) flip and CD intensity. The qualitative and quantitative analysis of the surface current distribution of chiral enantiomers reveals that the chirality of meta-atoms originates from the surge of electric dipole p_x and electric quadrupole Q . It is worth mentioning that the proposed strategy to achieve reconfigurable chirality using 3D morphological transformations can be directly extended to other higher frequencies, such as visible, infrared, and terahertz bands. Significantly, our paradigm to study the relationship between complex 3D morphology and chirality holds potential for application in biosensing, spin detection, and spin-selective devices. © 2023 Chinese Laser Press

<https://doi.org/10.1364/PRJ.480979>

1. INTRODUCTION

Chirality, the property of an object that is asymmetrical to its mirror image, plays an essential role in the chemical and biomedical fields. According to the Neumann–Curie principle [1], chiral materials possess some intrinsically unique properties due to structural symmetry breakings, such as circular dichroism (CD) [2–5] and linear polarization rotation. Among them, CD indicates that chiral materials can selectively absorb or transmit left-handed circularly polarized (LCP) and right-handed circularly polarized (RCP) electromagnetic (EM) waves. Many natural substances possess very weak chirality, such as DNA and proteins. Although most of their physical properties are identical, chiral objects and their enantiomers may exhibit different optical characteristics. Metamaterials are artificial materials designed to achieve a vast array of new functions and phenomena that are often unattainable with natural substances. A series of unique functions is realized by metamaterials, including polarization conversion

[6–10], holography [11–14], and orbital angular momentum [15–18].

Numerous metamaterials with strong chirality are also extensively studied to enhance the chirality. Usually, these metamaterials exhibit two types of optical chirality: extrinsic [19,20] and intrinsic [21,22]. Metamaterials with intrinsic chirality exhibit optical chirality for EM waves in any incident direction. In contrast, extrinsic chirality exists mainly in metamaterials with non-chiral structures. When the light wave is obliquely incident or tilted to the metamaterial, the system composed of the non-chiral metamaterial and the wave vector of the incident EM wave cannot coincide with its mirror image. Hence, the symmetry is broken, and the whole system possesses extrinsic chirality and exhibits chiral optical properties. A metasurface [23–25], the two-dimensional form of the metamaterial, usually possesses only extrinsic chirality and exhibits a planar chiral optical response. Extrinsic chirality is usually caused by electric dipole p and magnetic dipole m excited by the metasurface and can be observed when $p \cdot m \neq 0$. Reconfigurable chiral

metasurfaces in which active devices such as graphene [26,27] and diodes [28] are introduced to achieve chirality strength manipulation and chiral inversion have also been widely investigated. However, 2D metasurfaces exhibit weak and extrinsic chirality due to the lack of design freedom along the z axis. Therefore, 3D chiral metamaterials are used to achieve strong and intrinsic chirality. Strong chirality can be obtained by designing the morphology of 3D metamaterials to break the mirror symmetry, and these structures include helices [29,30] and twisted structures [31,32]. Simultaneously, the realization of reconfigurable 3D chiral metamaterials is significant for the real-time dynamic manipulation of chiral devices and can be widely used for sensing and detection. However, there are fewer strategies to achieve reconfigurable chirality of 3D metamaterials, the most widespread of which is the Kirigami/Origami technique [33–35]. However, Kirigami/Origami mainly requires the use of mechanical modulation, which is difficult to achieve precise and independent manipulation of individual unit cells.

Shape memory alloys (SMAs) [36,37], as a temperature-sensitive 3D morphologically reconfigurable material, are an excellent candidate for 3D reconfigurable chiral metamaterials. SMA appears as martensite at low temperatures and austenite at high temperatures. When the low-temperature martensite is heated, the SMA returns to the high-temperature austenite form, thus producing a transformation of the geometry. The SMA then returns to the martensitic form by releasing internal elastic energy during cooling. A nickel–titanium alloy [38,39] is a type of SMA with the advantages of wear resistance and super elasticity. Scientists have long recognized the enormous potential of SMA for scientific and engineering applications and have used SMA in a wide range of applications in medicine [40,41], architecture [42], aerospace [43], and robotics [44]. In addition, there is also a part of research to employ SMA for EM devices [45–47]. However, it is challenging to achieve continuous and fast modulation of SMA temperature in a natural environment since SMA is sensitive to temperature.

Benefiting from the excellent 3D morphological memory property of SMA, we propose and validate a paradigm of morphologically reconfigurable 3D metamaterials with giant and reconfigurable chirality, as shown in Fig. 1. One layer of voltage-controlled heating film (blue part of the meta-atom) is applied to the SMA to achieve continuous and fast shape transformation of the SMA. A chiral enantiomer is formed exactly when the SMA is bent along the $+z$ direction and $-z$ direction, enabling chiral flipping, and the chirality of the meta-atom is strongly and positively correlated with the absolute value of the curvature of the SMA. The CD of the meta-atom was investigated by analyzing the transmission spectra and surface currents. The analysis of the surface currents also demonstrates that the feeding lines introduced by the proposed voltage-controlled strategy do not affect the chirality of the meta-atom. Furthermore, the scattered power of different multipole moments was investigated using multipole decomposition. The underlying physical mechanism behind chirality is revealed to lie mainly in the surge of electric dipole p_y and electric quadrupole Q . Compared to complex 3D or multi-layer fabricated chiral metamaterials, the controllable 3D

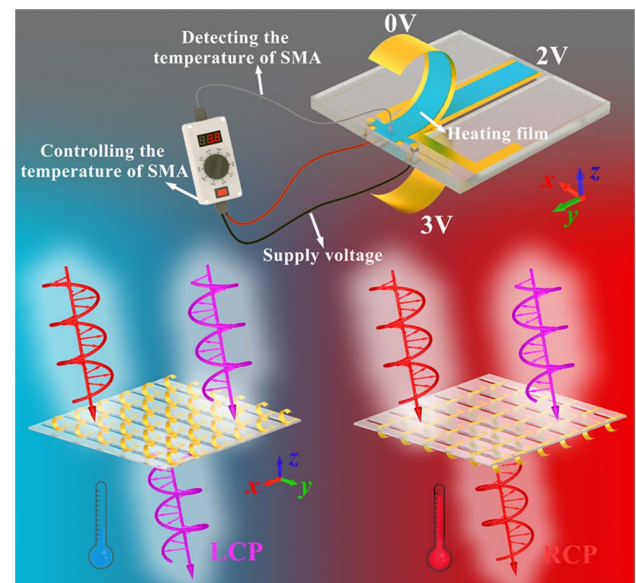


Fig. 1. Schematic diagram of the voltage-controlled 3D reconfigurable chiral metamaterial. The SMA is covered with a 0.1 mm thick insulating heating film, as shown in the blue part between the feeding vias and the SMA. The DC voltage source adjusts the voltage loaded on the heating film to achieve temperature control by detecting the difference between the temperature of the SMA and the target temperature.

morphological transformation strategy offers additional degrees of freedom for manipulating the spin of light in chiral metamaterials. SMA-based chiral materials may enable many attractive and profound applications in tailoring polarization, spin detection and selection, and biosensing.

2. RESULTS AND DISCUSSION

A. SMA-Based Chiral Metamaterial Design

An SMA sheet of 10 mm × 40 mm was fabricated and welded on the top of the F4B substrate to achieve chiral inversion and chiral strength modulation. Here, the relative permittivity of F4B at 3.5 GHz [$\epsilon_r = 4.3(1-0.025j)$] is used for simulation since the relative permittivity of F4B is almost constant at 3–4 GHz. The SMA sheet bends toward the $-z$ axis at high temperature and the $+z$ axis at low temperature with the same curvature; the curvature of the memory alloy sheet is temperature sensitive. Next, two completely different L-shaped metal patches were etched on each end of the SMA to break the mirror symmetry about all planes, as shown in Fig. 2(a). Note that the metal etched on the F4B substrate is copper with a thickness of 0.035 mm, except for SMA, which is made of a nickel–titanium alloy. Hence, the entire meta-atom is chiral when the SMA is bent in the $+z$ and $-z$ directions, which exactly forms the enantiomers (see Visualization 1). When the SMA does not bend, i.e., when the curvature of the SMA is zero, the meta-atom is mirror-symmetric about the xy plane, and the chirality of the meta-atom disappears at this time. The SMA is temperature sensitive, but continuous and rapid manipulation of ambient temperature is hard to achieve. Here, we adopt the strategy of covering the SMA with a heating film, which is

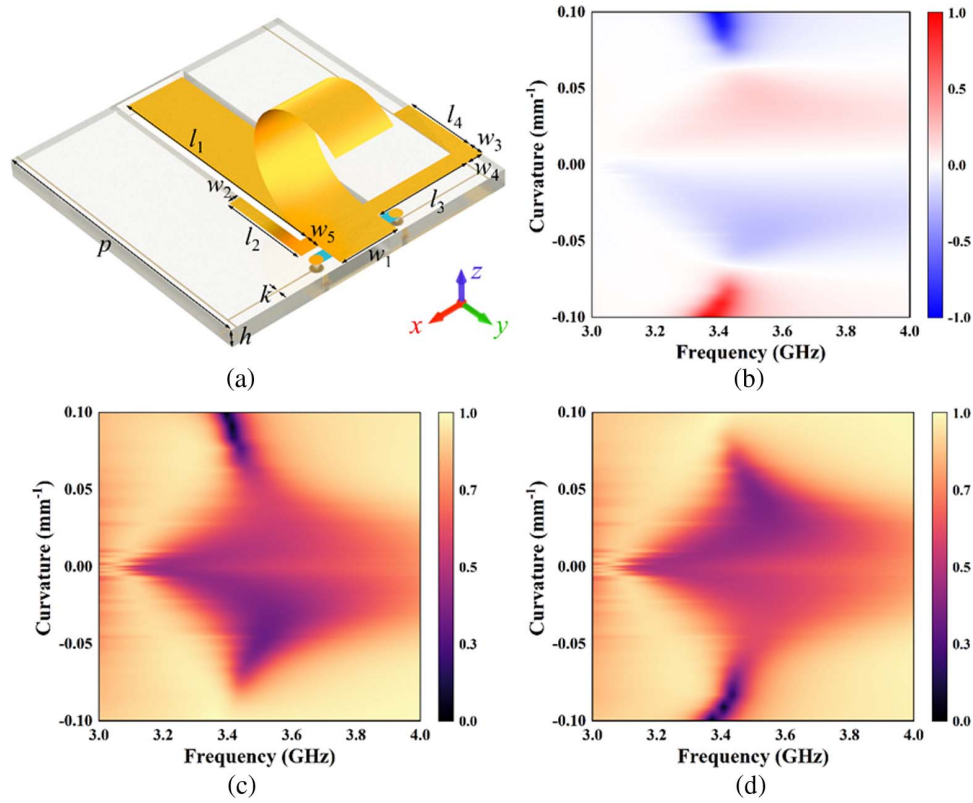


Fig. 2. Schematic diagram of the meta-atom and its transmission spectrum. (a) Schematic of the meta-atom; the optimized parameters are $p = 48$ mm, $l_1 = 39$ mm, $w_1 = 10$ mm, $l_2 = 15$ mm, $w_2 = 2$ mm, $l_3 = 16$ mm, $w_3 = 3$ mm, $l_4 = 12$ mm, $w_4 = 3$ mm, $w_5 = 2.5$ mm, $k = 0.2$ mm, $h = 1$ mm. (b) CD spectrum varying with SMA's curvature and frequency; transmission spectrum varying with SMA's curvature and frequency under (c) RCP and (d) LCP wave incidence. The positive (+z direction) or negative (-z direction) curvature indicates only the curving direction of SMA.

insulating and precisely controlled by the voltage. The heating film is fabricated by printing brass onto a polyimide film. The thickness of both brass and polyimide film is 0.05 mm, and the power of the heating film is 3.5 W. Two feeding lines are etched on the back side of the F4B substrate to supply voltage to the heating film and are connected to the positive and negative terminals of the heating film through vias. Here, the feeding lines have almost no effect on the chirality of the meta-atom since it is symmetric and very thin, which will be demonstrated in the subsequent discussion.

Next, the transmission coefficient of the meta-atom was simulated using the finite element numerical simulation software COMSOL Multiphysics. The boundary conditions along the x direction and y direction are periodic, and the boundary conditions along the z direction are open. It is evident that the meta-atom exhibits strong spin-selective transmission at 3.4 GHz. The chiral enantiomers exhibit completely opposite transmission effects under the same polarization incidence. For instance, the meta-atom is completely transparent to LCP wave incidence when the SMA's curvature $1/\rho = -0.1$ but completely opaque when $1/\rho = +0.1$. Here, CD is introduced to characterize the chirality of the meta-atom, and the CD is defined by co-polarized transmission coefficients: $CD = |t_{RR}|^2 - |t_{LL}|^2$ since the cross-polarized transmission

coefficients t_{LR} and t_{RL} are the same (see Fig. 7, Appendix B), where t_{RR} (t_{LL}) represents the transmission coefficient of the transmitted RCP (LCP) wave at the incidence of the RCP (LCP) wave. The calculated CD spectrum is shown in Fig. 2(b), and it is clear that the chirality of the meta-atom is strongly correlated with $1/\rho$ [48]. Visualization 2 shows the dynamic change of CD with curvature. However, the correlation between them is not strictly proportional.

B. Analysis of Chirality

In the subsequent content, the surface current distribution of the meta-atom simulated in COMSOL can better help reveal the underlying mechanism of chirality. Note that the red arrow in Fig. 3 represents only the direction of the surface current, and the intensity of the surface current is represented by the color map. By comparing the surface currents at different curvatures and different polarized wave incidences, it can be seen that when the transmission of a certain polarization wave is poor, the strong surface current is generated on the meta-atom at the incidence of such polarized wave, as shown in Figs. 3(a) and 3(f). When $1/\rho = +0.1$, the surface currents formed at the connection of SMA and arm I and at the corner of arm II are the strongest under RCP wave incidence. The surface current formed on arm I is along the $+y$ direction, while the

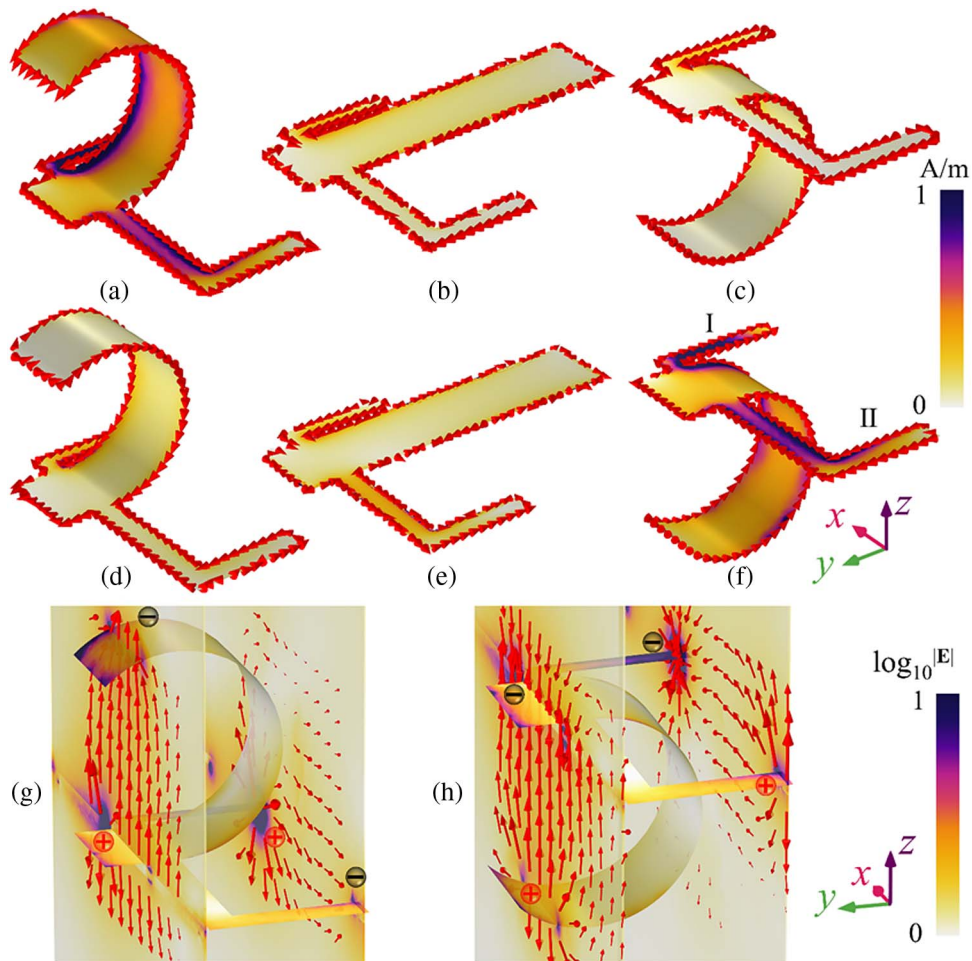


Fig. 3. Surface current distribution when (a) $1/\rho = +0.1$, (b) $1/\rho = 0$, and (c) $1/\rho = -0.1$ under RCP wave incidence; surface current distribution when (d) $1/\rho = +0.1$, (e) $1/\rho = 0$, and (f) $1/\rho = -0.1$ under LCP wave incidence. Electric field distributions ($\log_{10}^{|E|}$) around a meta-atom under (g) RCP wave and (h) LCP wave incidence. Note that the surface currents given are obtained from the simulation with the feeding lines, but the surface currents on the feeding lines are not given here for clarity.

surface current on arm II is along the $-x$ and $-y$ directions, so the electric dipole along the y direction is cancelled, and strong electric dipole p_x is formed in the x direction. The upward loop current is formed on the curved SMA, which generates strong electric dipole p_z in the z direction since the y component of the loop current is cancelled. Simultaneously, magnetic dipole m_z along the z direction is formed at the connection of SMA and arm I and the corner of arm II. Magnetic dipole m_x along the x direction is formed at the bent SMA. However, the magnetic dipoles generated are small since there is no closed-loop surface current. The intensity and direction of the electric field on the two cut surfaces of the meta-atom and the surface electric field intensity of the metal parts are given in Fig. 3(g). Apparently, there are four positions where the electric field strength is strongest and can be equated to the source and sink of the electric field. In other words, these four locations can be equated to two positive and two negative charges, as shown in Fig. 3(g). Hence, these two pairs of charges form electric quadrupole Q . Here, toroidal dipole T and magnetic quadrupole M are almost non-existent because of the weak magnetic dipole, and it is

difficult to form a circular magnetic dipole. Therefore, the meta-atom forms strong electric dipoles p_z and p_x , magnetic dipole m_z , and electric quadrupole Q when $1/\rho = +0.1$ under RCP wave incidence. Note that higher-order multipole moments are not considered here because their scattered powers are usually extremely weak. When $1/\rho = +0.1$, the intensity of the surface current excited by LCP wave incidence is extremely weaker than that excited by RCP wave incidence, which indicates that the designed meta-atom is transparent to the LCP wave but opaque to the RCP wave. Simultaneously, the direction of the surface current excited by LCP wave incidence is exactly opposite to that excited by RCP wave incidence. Hence, the strongest multipole moments excited under LCP wave incidence are also p_z , p_x , m_z , and Q , but they are all very weak in energy.

In the following, the surface current when the meta-atom chirality disappears at $1/\rho = 0$ is analyzed. Apparently, the surface currents excited by RCP wave incidence and LCP incidence are almost identical, which indicates the disappearance of the spin selectivity of the meta-atom. The surface currents

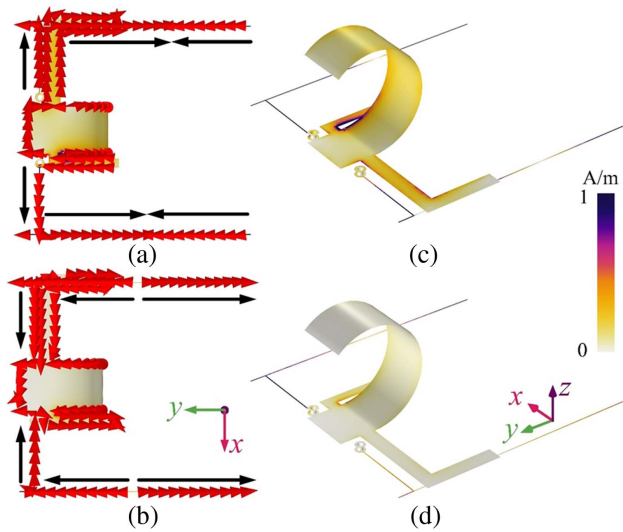


Fig. 4. Surface current distribution. The surface current direction under (a) RCP wave incidence and (b) LCP wave incidence. The surface current intensity under (c) RCP wave incidence and (d) LCP wave incidence.

are disordered when $1/\rho = 0$, but mainly along the y direction, thus forming an electric dipole along y direction p_y . Next, it can be seen that the surface current when $1/\rho = -0.1$ is exactly opposite to the surface current when $1/\rho = +0.1$. The surface current excited under LCP wave incidence is strongest when $1/\rho = -0.1$. Similarly, the curved SMA forms a strong p_z , and the y direction surface currents on arm I and arm II cancel, resulting in a stronger p_x and weaker p_y . As mentioned previously, m , T , and Q are also weak in this case. The electric field distribution shown in Fig. 3(h) indicates there also exist four positions with strong electric field intensity and form two pairs of sources and sinks. Hence, strong electric quadrupole Q is also formed at this time. Here, the most significant multipole moments excited under LCP wave incidence are p_z , p_x , p_y , and Q when $1/\rho = -0.1$.

In the subsequent content, the influence of the feeding lines on the chirality of the meta-atom will be discussed. Here, only the case when $1/\rho = +0.1$ is discussed as an illustration, while the case when $1/\rho = -0.1$ is similar. In the design, the feeding lines are symmetrical and thin to minimize the effect of the feeding lines on the chirality of the meta-atom. In this case, the surface currents excited under RCP incidence in y direction feeding lines are in opposite directions. Therefore, the excited electric dipole moments also cancel out. In addition, the surface currents on x direction feeding lines are opposite and therefore do not excite dipoles. Overall, the surface current excited on the feeding lines does not contribute to the dipole of the meta-atom. Simultaneously, the strong surface currents on the feeding lines are excited with both RCP incidence and LCP wave incidence, as shown in Figs. 4(c) and 4(d). Hence, the feeding lines have the same interaction for both RCP and LCP waves. As a verification, we give the transmission coefficient of the meta-atom with and without feeding lines when $1/\rho = +0.1$, as shown in Fig. 8(b). By comparison, it is found that the feeding lines do not affect the chirality of

the meta-atom, but the strong surface current excited by it will affect the resonant frequency of the meta-atom.

Furthermore, the scattering powers of multipole moments excited at the incidence of RCP and LCP waves were calculated separately to verify the above qualitative analysis. Here, the multipole decomposition is performed to quantify their contribution. The scattered power of the multipole moments can be obtained by integrating over the charge density $\rho(\mathbf{r}, t)$ in the Cartesian coordinate system. Here, the charge density $\rho(\mathbf{r}, t)$ and current density $\mathbf{J}(\mathbf{r}, t)$ satisfy the continuity equation [49]

$$\frac{\partial \rho(\mathbf{r}, t)}{\partial t} + \text{div} \mathbf{J}(\mathbf{r}, t) = 0. \quad (1)$$

By integrating the surface currents, the scattered power of the multipole moment can be obtained by [49–51]

$$\begin{aligned} I = & \frac{2\omega^4}{3c^3} |P|^2 + \frac{2\omega^4}{3c^3} |M|^2 + \frac{4\omega^5}{3c^4} (P \cdot T) + \frac{2\omega^6}{3c^5} |T|^2 \\ & + \frac{\omega^6}{5c^5} \sum |Q_{\alpha\beta}|^2 + \frac{\omega^6}{40c^5} \sum |M_{\alpha\beta}|^2 + \frac{2\omega^6}{15c^5} (M \cdot \langle R_M^2 \rangle) \\ & + o\left(\frac{1}{c^5}\right). \end{aligned} \quad (2)$$

The terms of the equation represent, in order, electric dipole (charge) and magnetic dipole scattering, interference between electric dipole and toroidal dipole, toroidal dipole scattering, scattering of electric quadrupole and magnetic quadrupole, and further corrections caused by interference between magnetic dipole and the first-order mean square radius of the magnetic dipole distributions. The third and last two terms are several orders of magnitude lower than the other terms and are therefore ignored. More calculation details are shown in Appendix A. The quantitative results of the calculations are shown in Fig. 5, which matches well with the qualitative analysis discussed above. It can be seen that multipole moments with dominant scattered power excited at RCP wave incidence are p_z , Q , p_x , and m_z when $1/\rho = +0.1$, as shown in Fig. 5(a). However, p_z and m_z do not contribute to the transmission of the meta-atom since the EM waves are incident along the $+z$ axis. Hence, electric quadrupole Q and electric dipole p_x play a dominant role. Simultaneously, it is noted that the power scattered by multipole moments at LCP wave incidence is extremely small compared to that at RCP wave incidence, which is caused by the weak surface current. By comparing the scattered power of multipole moments at $1/\rho = +0.1$ and $1/\rho = -0.1$, the two cases are exactly opposite. When $1/\rho = -0.1$, the power scattered by multipole moments at LCP wave incidence is maximum, and also Q and p_x play a dominant role, as shown in Fig. 5(f). When the meta-atom is in the non-chiral state, the powers scattered by multipole moments are the same under both polarization incidences. Electric dipole p_y plays a dominant role and deteriorates the transmission of both RCP and LCP waves, which coincides with the qualitative analysis. More analysis of Q can be found in Appendix D. In conclusion, quantitative multipole decomposition shows that the chirality of the meta-atom lies with a different response to CP waves with different spins, resulting in

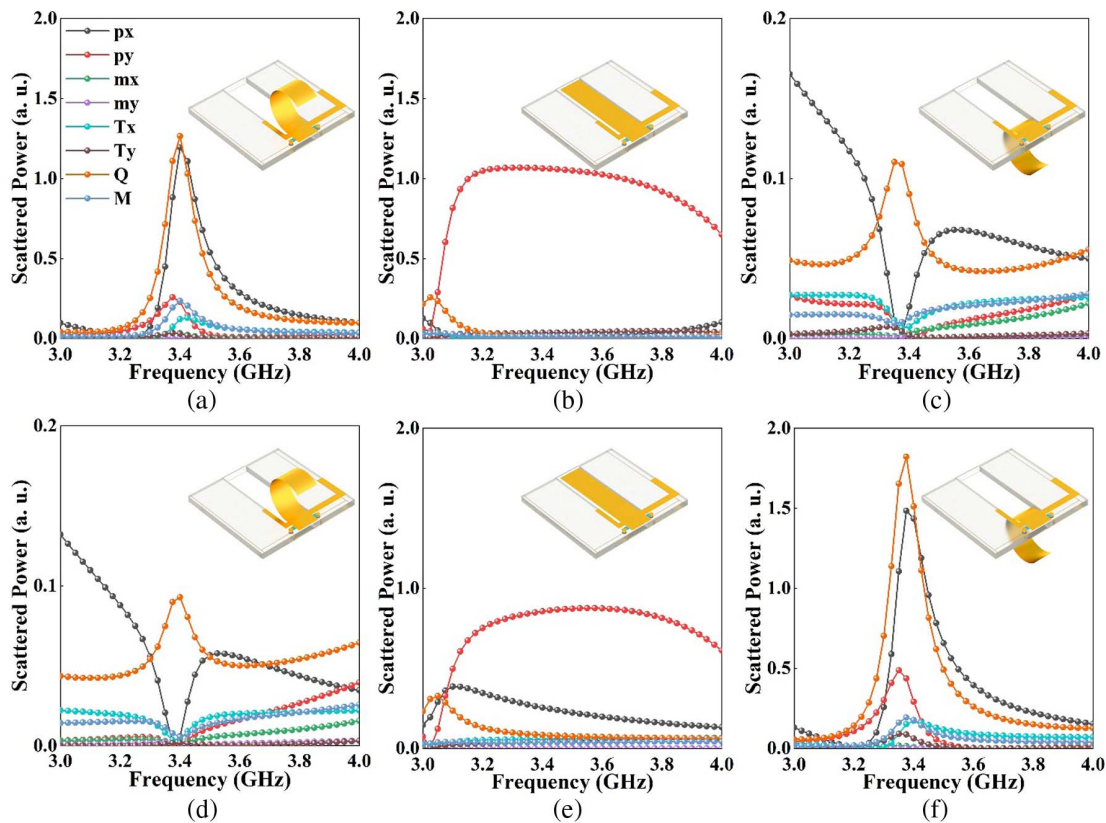


Fig. 5. Amplitudes of the power scattered by multipole moments. Power scattered by multipole moments under RCP wave incidence when (a) $1/\rho = +0.1$, (b) $1/\rho = 0$, and (c) $1/\rho = -0.1$. Power scattered by multipole moments under LCP wave incidence when (d) $1/\rho = +0.1$, (e) $1/\rho = 0$, and (f) $1/\rho = -0.1$.

strong dichroism. Here, the surge of scattered power of electric quadrupole Q and electric dipole p_x leads to a strong chirality of the meta-atom.

3. EXPERIMENT AND VERIFICATION

To further validate our design, the F4B substrate was fabricated by commercial printed circuit board technology, and SMA was welded on the F4B substrate. As shown in Fig. 6(a), the size of the prototype is 288 mm × 310 mm, and two feeding lines are located at the two ends of the array and are used as positive and negative poles. By setting the target temperature, the heating film can heat the SMA and dynamically adjust the voltage loaded on the heating film through the feedback mechanism of the temperature controller to achieve precise and stable control of the SMA temperature. Here, the time taken to bend the SMA from the $+z$ axis to the $-z$ axis is 21 s, and the consumed time of a bent SMA that recovers to its initial state is 159 s. The time response of the SMA can be improved by lowering the phase transition temperature and increasing the power of the heating film. The fabricated prototype is placed between a pair of S-band CP horn antennas in the microwave chamber to test transmission performance. Note that the S-band CP horn antenna can transmit and receive LCP and RCP waves, respectively, through a different subminiature version A (SMA). Two ports of Agilent's vector network analyzer (VNA) E8363B

are connected to the CP horn antennas, which are used as a transmitter and a receiver. The transmission coefficients of LCP and RCP waves were tested when the meta-atom was in two strong chiral states and a non-chiral state, respectively. The flipping of the CD and the arbitrary control of the CD strength are realized by setting different temperatures, and the test results are shown in Figs. 6(b)–6(d), which indicates that the measurement results coincide well with the simulation results. However, the resonant frequency is shifted, which may be because of the following reasons: (1) the dielectric constant of F4B used for processing is different from that used in simulation; (2) the curved SMA is not strictly circular. More measurement results are shown in Figs. 8(c) and 8(d), Appendix C.

4. CONCLUSION

In conclusion, we have experimentally demonstrated an SMA-based strategy for achieving reconfigurable intrinsic chirality through 3D morphological transformations, which is promising in reconfigurable optical meta-devices. The giant and reconfigurable chirality of the meta-atom is achieved by curved SMA, and the simulation results are in good agreement with the experimental results. The direction and degree of SMA bending make the meta-atom exhibit distinct transmissions for LCP and RCP waves, enabling the CD to switch arbitrarily

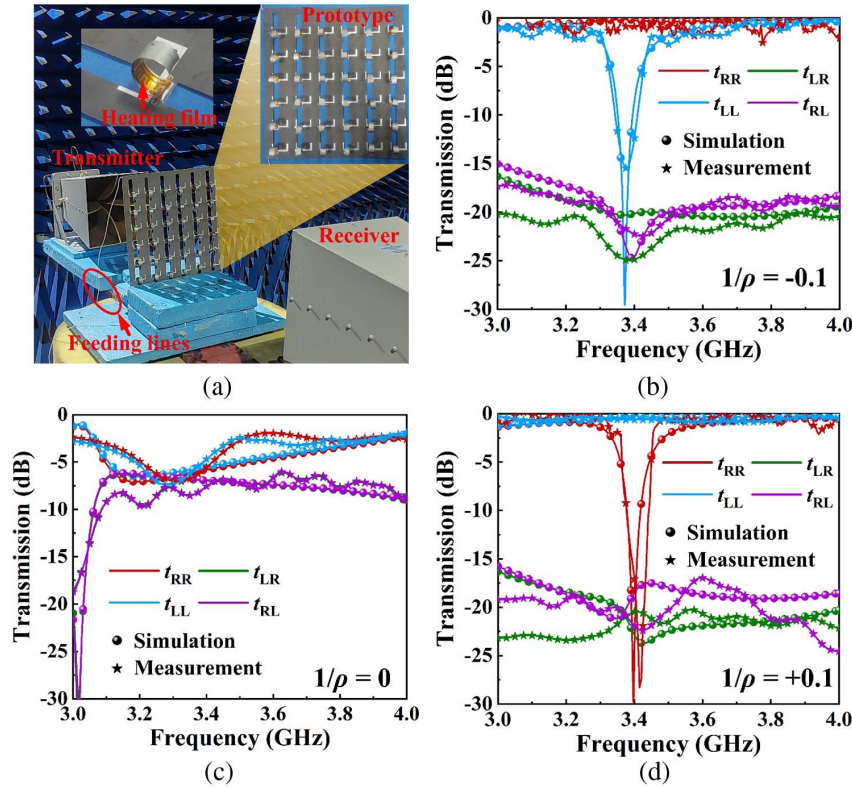


Fig. 6. (a) Measurement setup. Simulated and measured transmission performance under LCP and RCP waves incidence when (b) $1/\rho = -0.1$, (c) $1/\rho = 0$, and (d) $1/\rho = +0.1$.

between -1 and $+1$. The underlying physical mechanism of chirality was revealed through detailed analysis of excited electric dipole, magnetic dipole, and electric quadrupoles. The broadband chiral response can be achieved by introducing more resonant frequencies through adding symmetry-breaking structures. However, SMAs inevitably introduce losses at higher frequencies, which decrease the strength of CD and weaken the chirality of the meta-atom. The proposed strategy is simple, robust, actionable, and controllable in real time, which may be extended to terahertz and optical systems. Encouragingly, the proposed strategy holds promise for applications in areas such as biosensing and spin detection and selection.

APPENDIX A: CALCULATION OF SCATTERED POWER OF MULTIPOLE MOMENTS

The scattered power of multipole moments can be represented in the Cartesian coordinate system as follows [3]:

$$\text{electric dipole moment: } P_{\alpha} = \int d^3r \rho r_{\alpha} = \frac{1}{i\omega} \int d^3r J_{\alpha}, \quad (\text{A1})$$

$$\text{magnetic dipole moment: } M_{\alpha} = \frac{1}{2c} \int d^3r [\mathbf{r} \times \mathbf{J}]_{\alpha}, \quad (\text{A2})$$

$$\text{toroidal dipole moment: } T_{\alpha} = \frac{1}{10c} \int d^3r [(\mathbf{r} \cdot \mathbf{J})r_{\alpha} - 2r^2 J_{\alpha}], \quad (\text{A3})$$

electric quadrupole moment:

$$Q_{\alpha,\beta} = \frac{1}{i2\omega} \int d^3r [r_{\alpha} J_{\beta} + r_{\beta} J_{\alpha} - \frac{2}{3} \delta_{\alpha,\beta} (\mathbf{r} \cdot \mathbf{J})], \quad (\text{A4})$$

magnetic quadrupole moment:

$$M_{\alpha,\beta} = \frac{1}{3c} \int d^3r [\mathbf{r} \times \mathbf{J}]_{\alpha} r_{\beta} + [\mathbf{r} \times \mathbf{J}]_{\beta} r_{\alpha}, \quad (\text{A5})$$

where c is the speed of light, \mathbf{r} is the distance vector from the origin to point (x, y, z) , $\mathbf{J}(\mathbf{r}, t)$ is the current density, and $\alpha, \beta = x, y, z$.

APPENDIX B: TRANSMISSION SPECTRUM OF CROSS-POLARIZED COMPONENTS

The transmission spectrum of cross-polarized components (t_{LR} and t_{RL}) is same, as shown in Fig. 7. The transmission coefficient of cross-polarization can reach a maximum of 0.5, when the chirality of the meta-atom is also the weakest. Hence, cross-polarized transmission coefficient does not reflect the chirality of the meta-atom.

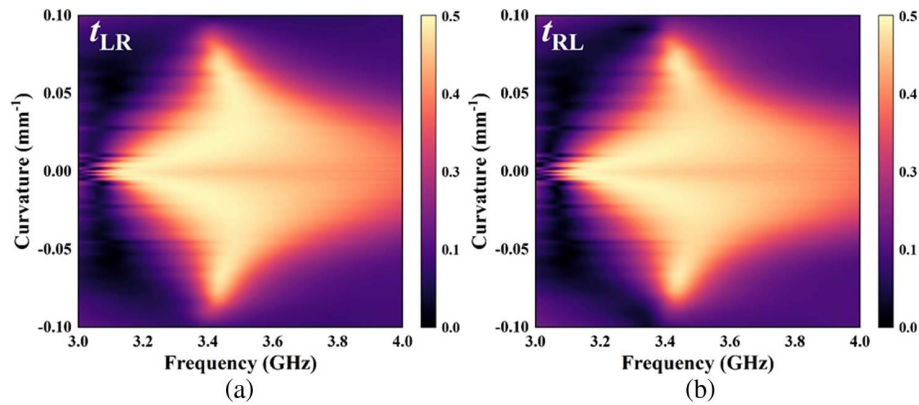


Fig. 7. Simulated transmission spectra of (a) t_{LR} and (b) t_{RL} vary with frequency and curvature.

APPENDIX C: RELEVANT RESULTS OF EXPERIMENTS AND SIMULATIONS

The time response of the metasurface is ultimately reflected in how fast the SMA's curvature changes. Here, a figure is given to depict the variation of the SMA's curvature with time to reflect the system's dynamics, as shown in Fig. 8. The factors that influence the curvature change during the heating (high voltage) process are the phase transformation temperature of the martensite and austenite of SMA, the ambient temperature, and the power of the heating film. The most dominant factor is the power of the heating film, which is controllable. The factors that influence the curvature change during the cooling (zero pressure) process are the phase transformation temperature

of the martensite and austenite of SMA and the ambient temperature. These two factors are both very difficult to change, so the time spent in the cooling process is much more than the time spent in the heating process. Also, the time response of the metasurface can be improved by lowering the phase transition temperature and increasing the power of the heating film.

APPENDIX D: ELECTRIC QUADRUPOLE MOMENT AND ITS COMPONENTS

Q_{ii} denotes the contribution of the charge system distributed on the i axis to the electric quadrupole, where $i = x, y, z$. Q_{ij} denotes the contribution of the charge system distributed in the ij plane to the electric quadrupole, where $i = x, y, z$.

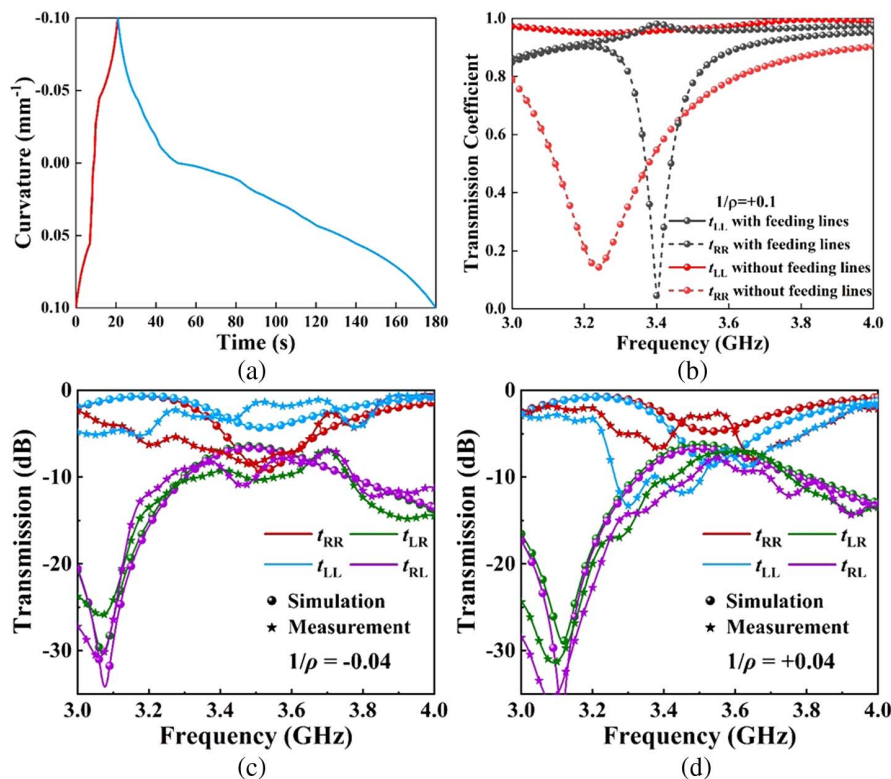


Fig. 8. (a) SMA's curvature varies with time. (b) Transmission coefficient of the meta-atom with and without feeding lines. Simulated and measured transmission performance under LCP and RCP waves incidence when (c) $1/\rho = -0.4$ and (d) $1/\rho = +0.4$.

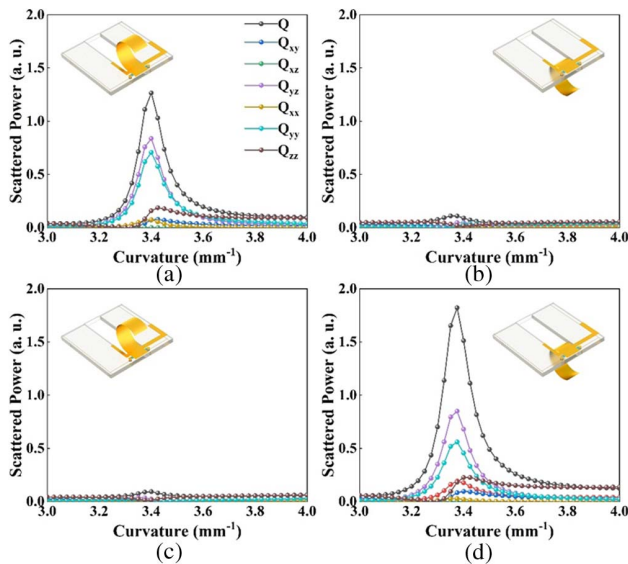


Fig. 9. The power scattered by Q under RCP wave incidence when (a) $1/\rho = +0.1$ and (b) $1/\rho = -0.1$. The power scattered by Q under LCP wave incidence when (c) $1/\rho = +0.1$ and (d) $1/\rho = -0.1$.

Here, each component of electric quadrupole Q contributes to the transmission of EM waves. Q_{yy} and Q_{yz} are the dominant components, as shown in Fig. 9.

Funding. National Natural Science Foundation of China (61971437, 61971341, 61971435); Natural Science Foundation of Shaanxi Province (2020JM-342, 2022JQ-630); Postdoctoral Science Foundation of China (2019M651644).

Disclosures. The authors declare no conflicts of interest.

Data Availability. The data that support the findings of this study are available from the corresponding author upon reasonable request.

[†]These authors contributed equally to this work.

REFERENCES

- D. S. Sanchez, I. Belopol'ski, T. A. Cochran, X. Xu, J. Yin, G. Chang, W. Xie, K. Manna, V. Süß, C. Huang, N. Alidoust, D. Multer, S. S. Zhang, N. Shumiya, X. Wang, G. Wang, T. Chang, C. Felser, S. Xu, S. Jia, H. Lin, and M. Z. Hasan, "Topological chiral crystals with helicoid-arc quantum states," *Nature* **567**, 500–505 (2019).
- Y. Li, Y. Pang, J. Wang, Q. Zheng, J. Zhang, J. Zhang, Y. Jing, L. Zheng, M. Feng, H. Wang, S. Qu, and T. Cui, "Tailoring circular dichroism in an isomeric manner: complete control of amplitude and phase for high-quality hologram and beam forming," *Adv. Opt. Mater.* **10**, 2101982 (2021).
- S. Yang, Z. Liu, S. Hu, A. Jin, H. Yang, S. Zhang, J. Li, and C. Gu, "Spin-selective transmission in chiral folded metasurfaces," *Nano Lett.* **19**, 3432–3439 (2019).
- A. Karabchevsky, "Single-shot circular dichroism spectroscopy," *Light Sci. Appl.* **11**, 133 (2022).
- L. Jiang, Y. Li, L. Zheng, H. Chen, Q. Yuan, Z. Zhu, H. Wang, Y. Pang, J. Wang, and S. Qu, "Temperature-adaptive reconfigurable chiral metamaterial for tailoring circular dichroism based on shape memory alloy," *Mater. Des.* **225**, 111496 (2023).

- S. Wang, Z. Deng, Y. Wang, Q. Zhou, X. Wang, Y. Cao, B. Guan, S. Xiao, and X. Li, "Arbitrary polarization conversion dichroism metasurfaces for all-in-one full Poincaré sphere polarizers," *Light Sci. Appl.* **10**, 24 (2021).
- L. Jiang, Y. Jing, Y. Li, W. Wan, Y. Cheng, L. Zheng, J. Wang, Z. Zhu, H. Wang, M. Feng, J. Zhang, and S. Qu, "Multidimensionally manipulated active coding metasurface by merging Pancharatnam-Berry phase and dynamic phase," *Adv. Opt. Mater.* **9**, 2100484 (2021).
- L. Jiang, Y. Li, L. Zheng, Q. Yuan, Z. Zhu, W. Wan, H. Wang, Y. Pang, J. Wang, W. Wang, T. Cui, and S. Qu, "Smart metasurface for active and passive cooperative manipulation of electromagnetic waves," *ACS Appl. Mater. Interfaces* **14**, 54359–54368 (2022).
- Y. Li, Y. Pang, J. Wang, Q. Zheng, M. Feng, H. Ma, J. Zhang, Z. Xu, and S. Qu, "Wideband polarization conversion with the synergy of waveguide and spoof surface plasmon polariton modes," *Phys. Rev. A* **10**, 064002 (2018).
- S. Zhang, L. Huang, G. Geng, J. Li, X. Li, and Y. Wang, "Full-Stokes polarization transformations and time sequence metasurface holographic display," *Photon. Res.* **10**, 1031–1038 (2022).
- Q. Xiao, Q. Ma, T. Yan, L. W. Wu, C. Liu, Z. X. Wang, X. Wan, Q. Cheng, and T. J. Cui, "Orbital-angular-momentum-encrypted holography based on coding information metasurface," *Adv. Opt. Mater.* **9**, 2002155 (2021).
- B. Xiong, Y. Xu, J. Wang, L. Li, L. Deng, F. Cheng, R. Peng, M. Wang, and Y. Liu, "Realizing colorful holographic mimicry by metasurfaces," *Adv. Mater.* **33**, 2005864 (2021).
- H. Ren, X. Fang, J. Jang, J. Bürger, J. Rho, and S. A. Maier, "Complex-amplitude metasurface-based orbital angular momentum holography in momentum space," *Nat. Nanotechnol.* **15**, 948–955 (2020).
- Y. Cheng, Y. Li, H. Wang, H. Chen, W. Wan, J. Wang, L. Zheng, J. Zhang, and S. Qu, "Ohmic dissipation-assisted complex amplitude hologram with high quality," *Adv. Opt. Mater.* **9**, 2002242 (2021).
- R. C. Devlin, A. Ambrosio, N. A. Rubin, J. P. B. Mueller, and F. Capasso, "Arbitrary spin-to-orbital angular momentum conversion of light," *Science* **358**, 896–901 (2017).
- R. Feng, B. Ratni, J. Yi, H. Zhang, A. de Lustrac, and S. N. Burokur, "Versatile metasurface platform for electromagnetic wave tailoring," *Photon. Res.* **9**, 1650–1659 (2021).
- Y. Shen, X. Wang, Z. Xie, C. Min, X. Fu, Q. Liu, M. Gong, and X. Yuan, "Optical vortices 30 years on: OAM manipulation from topological charge to multiple singularities," *Light Sci. Appl.* **8**, 90 (2019).
- Y. Jia, Y. Liu, B. Hu, W. Xiong, Y. Bai, Y. Cheng, D. Wu, X. Liu, and J. Christensen, "Orbital angular momentum multiplexing in space-time thermoacoustic metasurfaces," *Adv. Mater.* **34**, 2202026 (2022).
- E. Plum, X. Liu, V. A. Fedotov, Y. Chen, D. P. Tsai, and N. I. Zheludev, "Metamaterials: optical activity without chirality," *Phys. Rev. Lett.* **102**, 113902 (2009).
- E. Plum, V. A. Fedotov, and N. I. Zheludev, "Specular optical activity of achiral metasurfaces," *Appl. Phys. Lett.* **108**, 141905 (2016).
- X. Zhang, Y. Liu, J. Han, Y. Kivshar, and Q. Song, "Chiral emission from resonant metasurfaces," *Science* **377**, 1215–1218 (2022).
- F. Wu, Y. Tian, X. Luan, X. Lv, F. Li, G. Xu, and W. Niu, "Synthesis of chiral Au nanocrystals with precise homochiral facets for enantioselective surface chemistry," *Nano Lett.* **22**, 2915–2922 (2022).
- H. S. Khaliq, I. Kim, A. Zahid, J. Kim, T. Lee, T. Badloe, Y. Kim, M. Zubair, K. Riaz, M. Q. Mehmood, and J. Rho, "Giant chiro-optical responses in multipolar-resonances-based single-layer dielectric metasurfaces," *Photon. Res.* **9**, 1667–1674 (2021).
- A. Basiri, X. Chen, J. Bai, P. Amrollahi, J. Carpenter, Z. Holman, C. Wang, and Y. Yao, "Nature-inspired chiral metasurfaces for circular polarization detection and full-Stokes polarimetric measurements," *Light Sci. Appl.* **8**, 78 (2019).
- M. Cen, J. Wang, J. Liu, H. He, K. Li, W. Cai, T. Cao, and Y. J. Liu, "Ultra-thin suspended chiral metasurfaces for enantiodiscrimination," *Adv. Mater.* **34**, 2203956 (2022).
- Y. Meng, J. Fan, M. Wang, W. Gong, J. Zhang, J. Ma, H. Mi, Y. Huang, S. Yang, R. S. Ruoff, and J. Geng, "Encoding enantiomeric molecular chiralities on graphene basal planes," *Angew. Chem.* **61**, e202117815 (2022).

27. B. Zhao, S. Yang, J. Deng, and K. Pan, "Chiral graphene hybrid materials: structures, properties, and chiral applications," *Adv. Sci.* **8**, 2003681 (2021).
28. W. Wan, Y. Li, H. Wang, Z. Zhu, Y. Cheng, L. Jiang, L. Zheng, J. Wang, and S. Qu, "Chiral absorber-based frequency selective absorber with identical filtering characteristics for distinct polarizations," *IEEE Trans. Antennas Propag.* **70**, 3506–3514 (2022).
29. H. Po, C. Dabard, B. Roman, E. Reyssat, J. Bico, B. Baptiste, E. Lhuillier, and S. Ithurria, "Chiral helices formation by self-assembled molecules on semiconductor flexible substrates," *ACS Nano* **16**, 2901–2909 (2022).
30. X. Li, C. Ji, S. Chen, Y. Han, J. Liu, and J. Li, "Phase enabled circular dichroism reversal in twisted bi-chiral propeller metamolecule arrays," *Adv. Opt. Mater.* **9**, 2101191 (2021).
31. I. Fernandez-Corbaton, C. Rockstuhl, P. Ziemke, P. Gumbsch, A. Albiez, R. Schwaiger, T. Frenzel, M. Kadic, and M. Wegener, "New twists of 3D chiral metamaterials," *Adv. Mater.* **31**, 1807742 (2019).
32. C. Lin, C. Liu, Y. Chen, K. Chiu, J. Wu, B. Lin, C. Wang, Y. Chen, S. Chang, and Y. Chang, "Molecular chirality detection with periodic arrays of three-dimensional twisted metamaterials," *ACS Appl. Mater. Interfaces* **13**, 1152–1157 (2021).
33. Z. Wang, L. Jing, K. Yao, Y. Yang, B. Zheng, C. M. Soukoulis, H. Chen, and Y. Liu, "Origami-based reconfigurable metamaterials for tunable chirality," *Adv. Mater.* **29**, 1700412 (2017).
34. Z. Liu, H. Du, J. Li, L. Lu, Z. Li, and N. X. Fang, "Nano-kirigami with giant optical chirality," *Sci. Adv.* **4**, t4436 (2018).
35. Y. Tang, Z. Liu, J. Deng, K. Li, J. Li, and G. Li, "Nano-kirigami metasurface with giant nonlinear optical circular dichroism," *Laser Photon. Rev.* **14**, 2000085 (2020).
36. T. Omori and R. Kainuma, "Alloys with long memories," *Nature* **502**, 42–44 (2013).
37. P. Chowdhury and H. Sehitoglu, "Deformation physics of shape memory alloys-fundamentals at atomistic frontier," *Prog. Mater. Sci.* **88**, 49–88 (2017).
38. P. Hua, M. Xia, Y. Onuki, and Q. Sun, "Nanocomposite NiTi shape memory alloy with high strength and fatigue resistance," *Nat. Nanotechnol.* **16**, 409–413 (2021).
39. J. P. Oliveira, R. M. Miranda, and F. M. Braz Fernandes, "Welding and joining of NiTi shape memory alloys: a review," *Prog. Mater. Sci.* **88**, 412–466 (2017).
40. H. F. Li, F. L. Nie, Y. F. Zheng, Y. Cheng, S. C. Wei, and R. Z. Valiev, "Nanocrystalline $Ti_{49.2}Ni_{50.8}$ shape memory alloy as orthopaedic implant material with better performance," *J. Mater. Sci. Technol.* **35**, 2156–2162 (2019).
41. Y. Wang, J. Venezuela, and M. Dargusch, "Biodegradable shape memory alloys: progress and prospects," *Biomaterials* **279**, 121215 (2021).
42. M. Formentini and S. Lenci, "An innovative building envelope (kinetic façade) with shape memory alloys used as actuators and sensors," *Autom. Constr.* **85**, 220–231 (2018).
43. S. Li, D. Cong, W. Xiong, Z. Chen, X. Zhang, Z. Nie, S. Li, R. Li, Y. Wang, Y. Cao, Y. Ren, and Y. Wang, "A low-cost Ni–Mn–Ti–B high-temperature shape memory alloy with extraordinary functional properties," *ACS Appl. Mater. Interfaces* **13**, 31870–31879 (2021).
44. M. Han, X. Guo, X. Chen, C. Liang, H. Zhao, Q. Zhang, W. Bai, F. Zhang, H. Wei, C. Wu, Q. Cui, S. Yao, B. Sun, Y. Yang, Q. Yang, Y. Ma, Z. Xue, J. W. Kwak, T. Jin, Q. Tu, E. Song, Z. Tian, Y. Mei, D. Fang, H. Zhang, Y. Huang, Y. Zhang, and J. A. Rogers, "Submillimeter-scale multimaterial terrestrial robots," *Sci. Robot.* **7**, 107477 (2022).
45. C. Lor, R. Phon, M. Lee, and S. Lim, "Multi-functional thermal-mechanical anisotropic metasurface with shape memory alloy actuators," *Mater. Des.* **216**, 110569 (2022).
46. X. Chen, J. Gao, and B. Kang, "Achieving a tunable metasurface based on a structurally reconfigurable array using SMA," *Opt. Express* **26**, 4300–4308 (2018).
47. Y. Song and Y. Shen, "A metasurface radar for steering ultrasonic guided waves," *J. Sound Vib.* **538**, 117260 (2022).
48. A. Lakhtakia, V. K. Varadan, and V. V. Varadan, *Time-Harmonic Electromagnetic Fields in Chiral Media* (Springer-Verlag, 1989).
49. G. Vaman and E. E. Radescu, "Exact calculation of the angular momentum loss, recoil force, and radiation intensity for an arbitrary source in terms of electric, magnetic, and toroid multipoles," *Phys. Rev. E* **65**, 046609 (2002).
50. S. Linden, C. Enkrich, M. Wegener, J. Zhou, T. Koschny, and C. M. Soukoulis, "Magnetic response of metamaterials at 100 terahertz," *Science* **306**, 1351–1353 (2004).
51. T. Kaelberer, V. A. Fedotov, N. Papasimakis, D. P. Tsai, and N. I. Zheludev, "Toroidal dipolar response in a metamaterial," *Science* **330**, 1510–1512 (2010).